THE JOURNAL OF PHYSICAL CHEMISTRY C
A JOURNAL OF THE AMERICAN CHEMICAL SOCIETY

Open Access
This article is licensed under CC-BY-NC-ND 4.0

pubs.acs.org/JPCC Featured Article

Pulsed Force Kelvin Probe Force Microscopy—A New Type of Kelvin Probe Force Microscopy under Ambient Conditions

Amirhossein Zahmatkeshsaredorahi,‡ Devon S. Jakob,‡ and Xiaoji G. Xu*

Cite This: *J. Phys. Chem. C* 2024, 128, 9813−9827

Read Online

ACCESS | Metrics & More | Article Recommendations

ABSTRACT: Kelvin probe force microscopy (KPFM) is an increasingly popular scanning probe microscopy technique used for nanoscale imaging of surface potential for various materials, such as metals, semiconductors, biological samples, and photovoltaics, to reveal their surface work function and/or local accumulation of charges. This featured review outlines the operation principles and applications of KPFM, including several typical commercially available variants. We highlight the significance of surface potential measurements, present the details of the method operation, and discuss the causes of the limitation on spatial resolution. Then, we present the pulsed force Kelvin probe force microscopy (PF-KPFM) as an innovative improvement to KPFM, which provides an enhanced spatial resolution of <10 nm under ambient conditions. PF-KPFM is promising for the characterization of heterogeneous materials with spatial variations of electrical properties. It will be especially instrumental for investigating emerging perovskite photovoltaics, heterogeneous catalysts, 2D materials, and ferroelectric materials, among others.

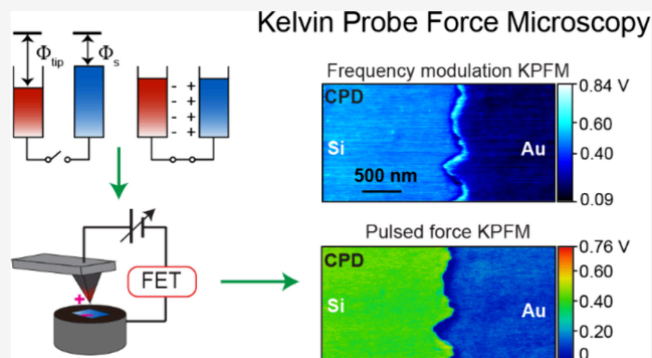

INTRODUCTION

The atomic force microscope (AFM)[1] is a robust and useful platform for measuring surface topography at the nanometer scale. However, topographic information alone often falls short of meaningful characterizations of complex and heterogeneous materials. For metals and semiconductors, quantifying the work function can provide additional information on the electrical and chemical properties.[2,3] For this purpose, Kelvin probe force microscopy (KPFM) is used as a nanoscale work function characterization and mapping technique. Since its introduction by Nonnenmacher, O'Boyle, and Wickramasinghe in 1991,[4] KPFM has become a widely adopted and versatile technique for measuring the work function of a wide range of materials, including semiconductors,[5] ferroelectrics,[6] perovskites,[7,8] biological/organic materials,[9] and dielectrics.[10] In this review, we present the fundamental principles of KPFM, including two popular commercially available variants of KPFMs, and the recently developed pulsed force KPFM, as well as discuss the outlook on KPFM methodologies for chemical research.

OPERATIONAL PRINCIPLES OF KPFM

For metals, KPFM measures their work function Φ, which is defined by eq 1 as the amount of energy needed to remove one electron from its Fermi energy, E_F, and place it in the vacuum state immediately outside of the material, with an energy E_V:

$$\Phi = E_V - E_F \tag{1}$$

The work function usually has the unit of eV. The work function is a surface property; as an estimation, only the ~5 outermost atomic layers contribute to a material's work function.[11] Therefore, the work function is sensitive to surface defects and chemistry (*e.g.*, surface contaminants, oxide layers, adsorbed moisture).[12,13] Surface temperature and crystal orientations also contribute to variations in the work function.[14,15] Measurement of work functions is useful for monitoring the effects of contaminants, doping, and crystal defects/interfaces on materials' electrical properties.

Lord Kelvin (William Thomson) invented the experimental method to measure work function at the macroscopic level in 1898,[16] which hence bears his name. The idea is depicted schematically in Figure 1a. Two dissimilar metal plates are placed parallel, separated by a small distance. When they are connected by a conducting wire, electrons spontaneously migrate from one plate to the other, leaving spatial separation of positive and negative charges.[17] This process is known as

Received: March 5, 2024
Revised: May 27, 2024
Accepted: May 28, 2024
Published: June 8, 2024

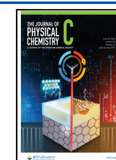

© 2024 The Authors. Published by American Chemical Society

https://doi.org/10.1021/acs.jpcc.4c01461
J. Phys. Chem. C 2024, 128, 9813−9827

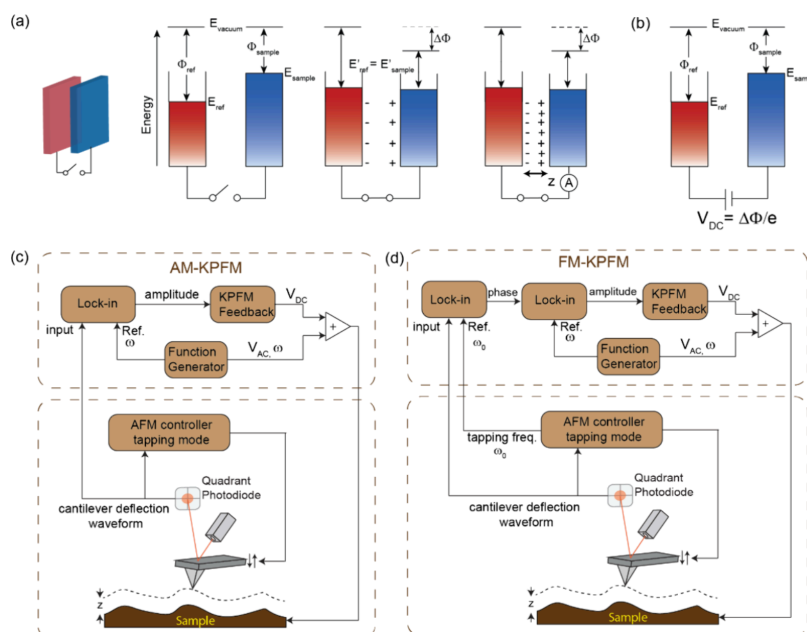

Figure 1. (a) Schematic illustration of the physical mechanism of the Kelvin probe method. Two metal plates (*i.e.*, reference and sample) with different Fermi levels are separated by distance z. Electrical connection results in migration of electrons and Fermi level alignment. Consequently, equal and opposite charges appear on each metal, which shifts the Fermi level and vacuum level of each plate. Work function Φ remains the same. If the distance z between two plates is modulated, an AC current will appear due to the modulation of the capacitance of the plates. (b) Electron migration between the plate and sample can be nullified or prevented by applying an external V_{DC} equal to $\Delta\Phi/e$. (c) Schematic representation of the construction of AM-KPFM. (d) Schematic representation of the construction of FM-KPFM that sequentially employs two lock-in amplifiers.

Fermi-level equalization. The spatial generated charges establish an electrical potential that causes the Fermi levels of both metal plates to align at the same energy. The value of this electrical potential (in volts) equals the difference in the work functions (in eV) of the two metallic plates divided by the unit charge. Fermi-level equalization causes the vacuum levels to shift, and the individual work functions of the plate remain unchanged.

When the distance between the two metal plates is modulated, the capacitance of the plate pair is also modulated accordingly. The number of electron migrations to maintain the needed electrical potential to achieve Fermi-level equalization is also modulated. Consequently, if we periodically modulate the distance between two plates, an alternating current (AC) will emerge, which is detectable with an ammeter. If an external DC voltage V_{DC} that equals the difference in work functions $\Delta\Phi$ divided by the unit charge e is applied between the two plates, Fermi levels are aligned by the externally applied electrical potential. Electron migration will be absent (Figure 1b). In the macroscopic Kelvin probe method, a metal plate of a known material (Kelvin probe) vibrates close to the sample of unknown material. The external DC voltage V_{DC} is scanned to search for a value that makes the AC current zero. This value of DC voltage V_{DC} is the contact potential difference (CPD) and is equal to $\Delta\Phi/e$ between the Kelvin probe and the sample.

Micro- and nanoscale measurements of work function remained elusive for almost a century following Lord Kelvin's original idea until the arrival of the AFM. The AFM allows for convenient nanoscopic positioning between a sharp metallic tip and a sample and, more importantly, detection of nano- to piconewton-level forces between them.[1,18] The AFM-based Kelvin probe method is called Kelvin probe force microscopy (KPFM), also known as scanning Kelvin probe microscopy (SKPM). Nonnemacher et al.,[4] first demonstrated KPFM that integrated a feedback loop to an electric force microscopy (EFM).[19] The main difference between the AFM-based KPFM from the macroscopic Kelvin probe method is that the capacitance between the AFM tip and sample is significantly smaller than that of the macroscopic Kelvin probe and plate sample. As a result, the electrical current due to charge migrations between the tip and sample due to Fermi level alignment is too small to be directly detected. Instead, in KPFM, an external AC voltage is applied between the tip and sample. The Coulombic force between the AFM tip and the sample emerges due to the charge migrations from the intrinsic difference in Fermi levels and externally applied voltage. The Coulombic force causes the AFM cantilever to bend or oscillate in the case of external AC voltage. The KFPM uses cantilever oscillations as a measurable quantity, as an AFM is good at measuring cantilever oscillations, particularly with lock-in detection.

The Coulombic force f between the AFM tip and a sample depends on the capacitance C between the tip and sample, and the voltage V between the tip and sample. When the tip−sample distance is defined as z, the Coulombic force is a negative gradient of the electrical potential energy $U = 1/2\ CV^2$. eq 2 shows the expression of Coulombic force:

$$f = -\frac{dU}{dz} = -\frac{1}{2}\frac{\partial C(z)}{\partial z}V^2 \tag{2}$$

Here, we assume that the capacitance C between the tip and sample is dependent on the tip−sample distance z. Voltage V between the tip and sample equals the externally applied voltage V_{ext} minus the CPD V_{CPD}. $V = V_{ext} - V_{CPD}$. The externally applied voltage V_{ext} can have a time dependence if it contains an AC component V_{AC}, which means that the Coulombic force f can have a dependence on time t. Following

eq 2, we see that the Coulombic force f is zero, if the external applied voltage V_{ext} equals V_{CPD}, regardless of the exact value or functional form of the $\frac{\partial C(z)}{\partial z}$ term.

Note that the Coulombic force $f(t)$ is also dependent on the position of the tip on the sample surface, *i.e.*, $f(t, x, y)$ with x and y as the lateral coordinates. The position dependence stems from the spatial dependence of the $V_{CPD}(x, y)$, *i.e.*, the sample has a spatial variation of work function that leads to CPD having spatial variations. The tip−sample capacitance $C(x, y, z)$ is also position-dependent for the lateral coordinates x and y if the sample surface is not uniform. Here, for the sake of simplicity, we omit the lateral dependence of V_{CPD} and $\frac{\partial C(z)}{\partial z}$ in our model description.

Figure 1c schematically displays the method developed by Nonnemacher et al.,[4] which is later popularly known as the amplitude-modulation KPFM (AM-KPFM) and is widely available in commercial AFM instruments. In AM-KPFM, the externally applied voltage V_{ext} has two components: a DC voltage V_{DC} and an AC voltage $V_{AC}\ \sin(\omega t)$ at the angular frequency ω. These two voltages are summed and applied between the tip and sample with a summing circuit. $V_{ext} = V_{DC} + V_{AC}\ \sin(\omega t)$

The time-dependent force $f(t)$ is

$$f(t) = -\frac{1}{2}\frac{\partial C(z)}{\partial z}(V_{DC} + V_{AC}\sin(\omega t) - V_{CPD})^2 \tag{3}$$

Expansion of eq 3 leads to three terms of the Coulombic force: a DC term, an AC term modulated at ω by $\sin(\omega t)$, and a second-order AC term modulated at 2ω by $\sin^2(\omega t)$. The AC terms of the Coulombic force cause the AFM cantilever to oscillate at corresponding frequencies. In AM-KPFM, the cantilever oscillations at the same frequency as the AC voltage are detected by a lock-in amplifier. The periodical force $f_\omega\ (t)$ at angular frequency ω (as a component of the overall $f(t)$) is expressed in eq 4:

$$f_\omega(t) = -\frac{\partial C(z)}{\partial z}(V_{DC} - V_{CPD})V_{AC}\sin(\omega t) \tag{4}$$

From eq 4, it is clear that if the externally applied V_{DC} equals to V_{CPD} between the tip material and the sample, the component of the Coulombic force f_ω would be nullified, *i.e.*, becoming zero, and the cantilever oscillation at ω will be suppressed.

AM-KPFM employs a negative feedback loop, *e.g.*, a Proportional-Integral-Derivative (PID) loop, to regulate the cantilever's oscillation amplitude at the angular frequency ω. In the AM-KPFM feedback, the cantilever's oscillation amplitude and phase from lock-in detection are treated as process variables. The feedback loop adjusts the DC component of the external voltage V_{DC} to minimize the oscillation amplitude to zero, which is the value of the set point. The V_{DC} is recorded as V_{CPD}. The diagram of AM-KPFM is shown in Figure 1c.

One key element in the treatment for Coulombic force generation is that the metallic tip and the sample form a capacitor, which means they are detached without contact. As such, the KPFM measurement requires the tip and sample to be separated by a finite distance. In a typical AM- KPFM operation under ambient conditions, this requirement is guaranteed to be satisfied using the lift mode operation. The AFM tip first scans a line of the topography, which is recorded by the AFM controller. Then, the AFM lifts its tip to a finite height, typically several tens of nanometers, and then traverses the same line following the recorded topography. The AC voltage modulation and KPFM feedback are active in the lift mode scan, and the feedback-regulated V_{DC} that minimizes the AC voltage-induced cantilever oscillation is recorded as the CPD. Spatial scanning of the AFM tip position and record V_{DC} under the KPFM feedback gives a map based on CPD.

Another increasingly popular and commercially available KPFM modality is the frequency modulation KPFM (FM-KPFM), introduced by Kitamura and Iwatsuki.[20] FM-KPFM also employs a negative feedback loop to search for CPD under externally applied V_{DC} and V_{AC}, however, the process variable to be regulated is from the shift of cantilever oscillation frequency, rather than amplitude. Figure 1d illustrates the construction of FM-KPFM.

A simple physical picture of FM-KPFM is the model of a damped-driven harmonic oscillator (*i.e.*, AFM cantilever) under a force gradient of Coulombic origin. In a nutshell, a damped harmonic oscillator's resonant frequency shifts if placed in a force gradient. When externally applied V_{DC} equals the CPD, the capacitor formed by the tip−sample junction is not electrically charged, and the Coulombic force is absent, and so is the gradient from the Coulombic force. However, if V_{DC} differs from the CPD, charges are present between the tip−sample junction, and as a result, the Coulombic force and its gradient appear, which causes the AFM cantilever to shift its mechanical resonant frequency. Detecting the shift of the cantilever's resonant frequency reveals if the V_{DC} fully compensates the CPD.

The following model can explain the relationship between the shift of the mechanical resonant frequency and the CPD. The resonant angular frequency ω_0 of the cantilever is expressed as $\omega_0 = \sqrt{\frac{k}{\mu}}$, where k is the spring constant of the cantilever with a unit of N/m; μ is the reduced mass of the cantilever. The presence of the force gradient $\frac{\partial f}{\partial z}$ from the Coulombic force is equivalent to a modification term to the spring constant k. The effective spring constant is thus $k + \frac{\partial f}{\partial z}$. The shift of the cantilever resonant angular frequency $\Delta\omega_o$ is expressed in eq 5:

$$\Delta\omega_o = \sqrt{\frac{k + \frac{\partial f}{\partial z}}{\mu}} - \sqrt{\frac{k}{\mu}} \approx \frac{\omega_0}{2k}\left(\frac{\partial f}{\partial z}\right) \tag{5}$$

Here, the approximation holds if $\frac{\partial f}{\partial z}$ is much smaller than k. Combining eq 3 with eq 5, we arrive at eq 6:

$$\Delta\omega_o = -\frac{\omega_0}{4k}\frac{\partial^2 C(z)}{\partial^2 z}(V_{DC} + V_{AC}\sin(\omega t) - V_{CPD})^2 \tag{6}$$

As eq 6 describes, $\Delta\omega_o$ is now dependent on ω, the angular frequency of the externally applied AC voltage. Expansion of eq 6 leads to several terms, one of which contains a modulation at the AC frequency ω, as expressed by eq 7:

$$\Delta\omega_{o,\omega} = -\frac{\omega_0}{2k}\frac{\partial^2 C(z)}{\partial^2 z}(V_{DC} - V_{CPD})V_{AC}\sin(\omega t) \tag{7}$$

The implication of eq 7 is that if a lock-in detection were used to demodulate the shift of cantilever resonant frequency $\Delta\omega_o$ at the external AC voltage drive frequency ω, the demodulated amplitude on $\Delta\omega_{o,\omega}$ would contain the term

https://doi.org/10.1021/acs.jpcc.4c01461
J. Phys. Chem. C 2024, 128, 9813−9827

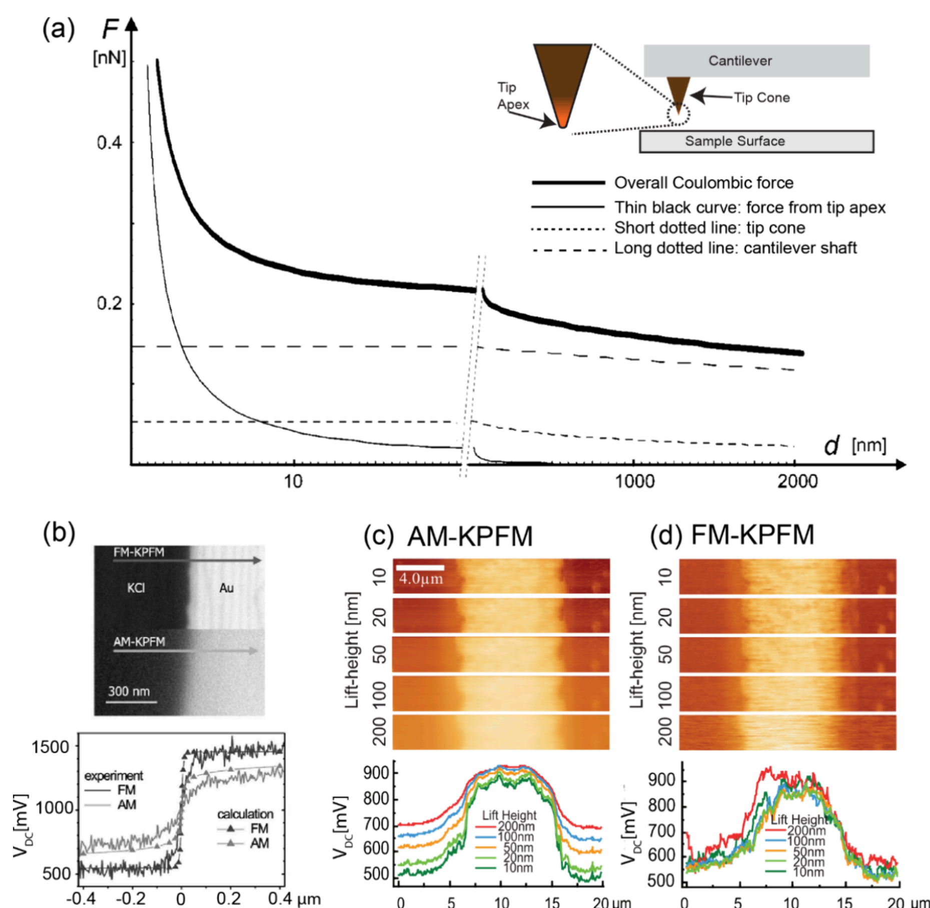

Figure 2. (a) Modeled electrostatic force between an AFM probe and a flat metallic surface as a function of tip−sample displacement. The total electrostatic force (thick line) is a convolution of forces originating from the tip apex (thin solid line), tip cone (short dotted line), and cantilever shaft (long dotted line). (b) KPFM images of a potassium chloride (KCl) island boundary on gold (Au). (top) FM-KPFM and AM-KPFM images were obtained across the boundary. (bottom) Simulated and experimental cross sections obtained across the KPFM images at the areas marked by the lines. (c, d) KPFM images were obtained with AM-KPFM and FM-KPFM at increasing lift heights. The measured CPD changes significantly with increasing lift heights with AM-KPFM. This effect is largely suppressed when using FM-KPFM. Panel (a) adapted with permission from ref 23. Copyright 2001 American Physical Society. Panel (b) adapted with permission from ref 27. Copyright 2005 American Physical Society. Panels (c, d) adapted with permission from ref 28. Copyright 2011 Institute of Physics Publishing.

$(V_{DC} - V_{CPD})$. If V_{DC} was equal to V_{CPD}, then the demodulated signal would become zero. However, the quantity $\Delta\omega_o$ is difficult to obtain experimentally, as it is an intrinsic property of the driven damped harmonic oscillator. When the cantilever is driven at the frequency ω_o, it oscillates at the frequency ω_o, despite the mechanical resonance may have been shifted to $\omega_o + \Delta\omega_o$ due to the force gradient. While it is possible to perform frequency sweeping to determine ω_o and calculate $\Delta\omega_o$ due to the presence of the Coulombic force, it is impractical to do so for every pixel of the FM-KPFM image. On the other hand, the oscillation phase ϕ_{ω_0} of the driven damped harmonic oscillator at the driving frequency ω_o is a readily accessible quantity from the lock-in output. A lock-in amplifier demodulates the cantilever's vertical deflection waveform at the driving frequency ω_o. The phase of the demodulation is then ϕ_{ω_0}. When the cantilever is driven at its resonance ω_o, the measured ϕ_{ω_0} is $\frac{\pi}{2}$ from the driving oscillation. When the cantilever is driven at ω_o, but the actual resonance is shifted to $\omega_o + \Delta\omega_o$ due to the force gradient, the value of ϕ_{ω_0} will differ from $\frac{\pi}{2}$. In the case of free space cantilever oscillation, if $V_{DC} = V_{CPD}$, then ϕ_{ω_0} should be $\frac{\pi}{2}$. However, when the tip is scanned on the sample surface, the intermolecular forces are present, and there is a pre-existing force gradient that already leads to the phase shift in ϕ_{ω_0} in the tapping mode oscillations. In order to identify the contribution to the phase shift from the externally applied AC voltage, the lock-in demodulated phase ϕ_{ω_0} is then routed into the second lock-in amplifier to be demodulated at the AC voltage frequency ω. The demodulation amplitude of the modulation on ϕ_{ω_0} is treated as the process variable of the FM-KPFM feedback. The PID controller of the feedback loop adjusts V_{DC} so that the demodulation on the cantilever phase ϕ_{ω_0} from the presence of external AC voltage of frequency ω is minimized. The regulated V_{DC} is thus equal to the CPD. A spatial scan of the AFM tip position and record V_{DC} under the FM-KPFM feedback loop gives the CPD map.

The lift mode operation is also used for the operation of FM-KPFM under ambient conditions, similar to that of the AM-KPFM. The AFM tip first scans a line of the topography of the sample, then is lifted to several tens of nanometers and repeats the recorded line profile. In the process, the average tip−sample distance remains the same. In the lift scan, the AFM cantilever is driven at its free-space resonant frequency

https://doi.org/10.1021/acs.jpcc.4c01461
J. Phys. Chem. C 2024, 128, 9813−9827

ω_0, while a combination of V_{DC} and V_{AC} voltages are applied between the tip and the sample under the feedback loop.

As estimated values, under ambient condition operation, cantilever free space resonant frequency is on the order of several hundred kHz; the AC voltage frequency is between 1–3 kHz; the magnitude of AC voltage is a few volts. The operation speed of FM-KPFM is much slower than that of AM-KPFM, as two lock-ins are used sequentially instead of one lock-in.

The lift mode operation is recommended for both AM- and FM-KPFM, because it avoids tip–sample contact when an external voltage is applied between the tip and sample. Otherwise, if the tip and the sample are in contact with a large external applied voltage, chances are detrimental side effects would happen, including thermal damages at the tip apex due to joule heating and electrochemical reactions on the sample. On piezoelectric samples, applying an external voltage between the tip and sample when they are in contact would excite the piezoelectric response as well,[21,22] which offers different physical properties from that of the KPFM.

However, the lift mode operation for ambient conditions AM- and FM-KPFM also comes at a price. Coulombic force is a long-range force that scales with $1/z^2$. When the tip is lifted to 50 nm or more, the Coulombic force contribution is no longer local to the apex of the metallic AFM tip of 20 nm or less radius of curvature. As a result, the collective Coulombic forces contain contributions from long-range sources, such as between the tip cone and the sample and between the cantilever shaft and the sample, in addition to the short-range source between the tip apex and the sample. Figure 2a displays the estimated contributions from these sources by Colchero et al.[23] When the tip is scanned across the sample surface, the force from the long-range sources barely changes, but they are nevertheless entered into the KPFM feedback. Consequently, the spatial resolution is significantly reduced due to the use of lift mode operation. On the other hand, between the AM-KPFM and FM-KPFM, the FM-KPFM gives better spatial resolutions because it is based on the derivative of the capacitance gradient $\frac{\partial^2 C(z)}{\partial^2 z}$, which scales with $1/z^3$. Stray capacitance that plagues the AM-KPFM contaminates FM-KPFM much less.[23−26] The detectable signal of FM-KPFM is more local than that of AM-KPFM. Figure 2b demonstrates the comparison of spatial resolutions,[27] which shows that the FM-KPFM has better spatial resolution than the AM-KPFM. The typical spatial resolution of FM-KPFM under ambient is about ∼50 nm with the lift mode. From the perspective of measurement accuracy, FM-KPFM is also more accurate than AM-KPFM. The contribution to tip–sample capacitance that is not from the tip apex is the stray capacitance that increases with the increase of the lift height. Stray capacitance affects the KPFM feedback and reduces its accuracy. AM-KPFM suffers more from stray capacitance. Figure 2c and 2**d** shows a comparison of the measured V_{DC} from AM- and FM-KPFMs, respectively, as lift height is increased. The measured values from FM-KPFM are less vulnerable to the change in lift height and remain the same within a hundred nanometers of lift height.[28]

However, the better accuracy and spatial resolution of FM-KPFM come at a price. The signal in FM-KPFM is often weak, and a high AC driving voltage is required to produce enough signal-to-noise (SNR) ratio. High AC driving voltages mean possible irreversible electrical damage if the tip and sample are accidentally in contact in the case of rough samples with low lift height. Also, the sequential utilization of two lock-in amplifiers reduces its operational speed. Lastly, the lift mode operation means that the same topography line is scanned twice (dual-pass), which inevitably means a longer measurement time compared to a single-pass line scan. On the other hand, the time spent for the first topography pass may be better utilized if the first pass is done with multimodal AFM mode such as the PeakForce Tapping QNM that gives both topography and mechanical information.[29] Bruker's PeakForce KPFM interleaves the peak force tapping topography line scan with the FM-KPFM in lift mode to deliver a multimodal characterization tool, albeit very slow.

Note that the drawback of the lift mode operation for AM-KPFM or FM-KPFM depends on how small the lift height is. Environmental vibrational noises are well isolated under ultrahigh vacuum (UHV) conditions with low temperatures. The lift height for KPFMs under UHV can be subnanometers, and the amount of AC voltage can be tens of millivolts. In such UHV conditions, FM-KPFM can achieve even subnanometer resolution with a metallic tip.[30,31]

The dual-pass operation of KPFM can also be avoided if the tapping mode AFM is operated in the noncontact mode (tapping in the attractive regime). In the attractive regime, the tip and sample are not in contact. Therefore, the externally applied AC voltage would not directly damage the sample surface, and the dual-pass lift mode can be avoided if the sample is not electrically sensitive. However, taping mode feedback on the attractive regime can be unstable or, to be more precise, "bi-stable",[32,33] thus leading to imaging artifacts that may compromise the nanoscale measurement. Another possibility of avoiding lift mode is to employ the peak force tapping mode and utilize the lift regime to implement AM-KPFM modulation, which results in the development of open-loop amplitude-modulation Kelvin probe force microscopy in single-pass peak force tapping mode by Stan and Namboodiri in 2022.[34] This method, similar to pulsed force KPFM that we developed in 2020, utilizes the detachment region of peak force tapping for KPFM measurement.

Besides AM- and FM-KPFMs, a promising route for fast and sensitive KPFM measurement in the tapping mode is the amplitude heterodyne KPFM, invented by Sugawara et al. in 2012.[35,36] Heterodyne KPFM utilizes two mechanical resonances of the cantilever. One is reserved for the tapping mode feedback, and the other is reserved for detecting the Coulombic force-induced cantilever oscillation. In heterodyne KPFM, the AC voltage V_{AC} is modulated at the frequency difference of the two mechanical resonances. The beating between the tapping mode driving frequency and the AC voltage driving frequency would result in an oscillation at the second mechanical resonance. This oscillation is dependent on the AC voltage driving, and its amplitude is amplified by the high Q-factor of the cantilever mechanical resonance. Similar to the AM-KPFM, a feedback loop on V_{DC} is used to minimize the cantilever oscillation amplitude due to the AC voltage to search for the CPD. Amplitude heterodyne KPFM's operation speed is on par with that of AM-KPFM, and its spatial resolution is similar to that of FM-KPFM.[36]

■ DESIRABLE TRAITS FOR KPFM UNDER AMBIENT CONDITIONS

A measurement tool's applications are intrinsically linked to its capability. There is an increasing need for nanoscale electrical

https://doi.org/10.1021/acs.jpcc.4c01461
J. Phys. Chem. C 2024, 128, 9813−9827

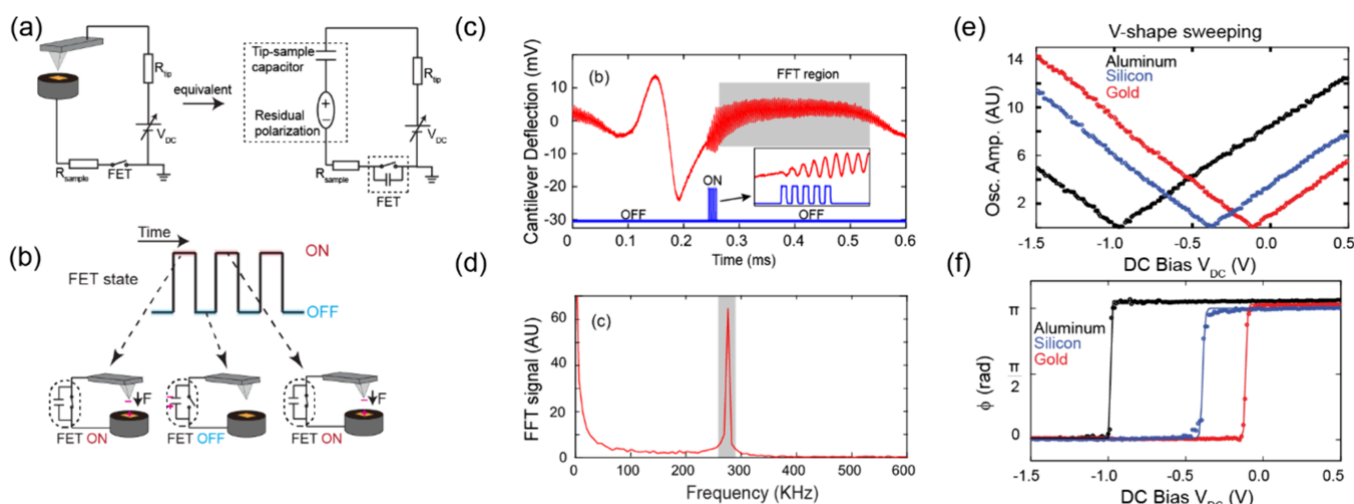

Figure 3. (a) Simplified presentation of PF-KPFM utilizing FET. Tip apex and sample surface form a nanocapacitor. This capacitance is in series with a residual polarization device which modifies the voltage base on Fermi Level difference and charge polarization on the surface. (b) Illustration of the role of the FET for mediation of electron migrations and opposite charges formation on the tip apex and sample surface during a FET switching process. (c) The Coulombic force generated between the tip and sample induces oscillation on the cantilever deflection curve with FET switching frequency, generating a PF-KPFM signal in the time domain. A peak in the frequency domain is obtained by using FFT on the signal region (gray rectangle). (d) FFT result of the oscillation in the frequency domain. Translating the signal from the time domain to the frequency domain via FFT results in a signal peak around the cantilever's free space resonance frequency. (e) Change in the oscillation amplitude during V_{DC} sweeping (V-shape plot) as the tip is stationary on top of the sample. The position of the tip is marked on Figure 4 panel (b) with colored dots (aluminum in black, silicon in blue, and gold in black). (f) Change in phase of the cantilever oscillation during V_{DC} sweeping. The CPD is equal to the external V_{DC}, which changes the oscillation phase by $\pi/2$. Panel (b) adapted with permission from ref 41. Copyright 2023 American Chemical Society. Panels (c−f) adapted with permission from ref 37. Copyright 2020 American Chemical Society.

measurement of work functions, Fermi levels and surface charges from emerging fields of photovoltaics, photocatalysts, and 2D materials. On the other hand, most of such materials are expected to be used under ambient conditions, under which their measurement should be performed. However, the AM- and FM-KPFMs have limited spatial resolution under ambient conditions. At a spatial resolution of ∼50 nm, commercially available FM-KPFMs are not powerful enough for the measurement of these emerging materials. While the AFM topography from a metal-coated tip can routinely reach ∼10 nm spatial resolution, one would desire ambient condition KPFM to also reach such resolution. This improvement would require the tip−sample distance to be kept small and ideally without lift mode. Moreover, the operation speed of the KPFM should be significantly increased so as to apply to reveal time-resolved dynamics. The dual-pass FM-KPFM is too time-consuming for fast screening of sample surfaces.

In the following sections, we summarize our continuous development of the pulsed force Kelvin probe force microscopy (PF-KPFM) since its invention in 2020.[37] This new method meets the above-discussed desirable traits for KPFM.

DEVELOPMENT OF PULSED FORCE KELVIN PROBE FORCE MICROSCOPY (PF-KPFM)

The main difference between the PF-KPFM and existing KPFM variants is the utilization of a field effect transistor (FET) to switch the electrical connectivity between the metallic tip and the sample rather than employing an externally applied V_{AC}. The motivation for using a FET to switch the electric connectivity is to bypass the limitation and distortion caused by the large amplitude V_{AC} required by ambient condition AM- or FM-KPFM. In fact, macroscopic Kelvin probe measurement has been implemented without an externally applied AC voltage.[38,39] In the PF-KPFM, the FET is used as a switchable electrical wire connecting the AFM tip and the sample, so that the Fermi level alignment between them causes electrons to migrate and generate Coulombic forces.[37] Because there is no external AC voltage, the operation of the PF-KPFM more resembles that of the Kelvin probe for the measurement of the potential at the sample surface. In a conceptually simplified schematic of PF-KPFM (Figure 3a), the sample surface of the tip−sample junction is electrically equivalent to a nanocapacitor in series with a voltage modification device that changes the electrical potential of the lower plate of the nanocapacitor. Such a voltage modification results from two possible contributions: (a) differences in the Fermi levels between the tip material and the sample material; (b) surface residual charges on the sample. Note that the surface residual charges often have accumulated countercharges near them on the surface or beneath the surface, which translates into the scenario of charge polarization rather than isolated charges. The external DC voltage V_{DC} is adjusted so that the electrical potential of the upper plate of the nanocapacitor matches that of the lower plate.

When the FET is switched ON, the tip and sample are electrically connected with low resistance. The difference in their work functions causes electrons to migrate, and the tip and sample adopt electrical charges. The presence of electrical charges changes the electric potential, which causes the vacuum level to shift and aligns the Fermi levels of the metallic tip and the sample (Figure 1a). As a result, a Coulombic force between the tip and sample appears, with magnitude proportional to the tip−sample work function difference. The force is expressed as eq 8:

$$f = -\frac{1}{2}\frac{\partial C(z)}{\partial z}(V_{DC} - V_{CPD})^2 \tag{8}$$

https://doi.org/10.1021/acs.jpcc.4c01461
J. Phys. Chem. C 2024, 128, 9813−9827

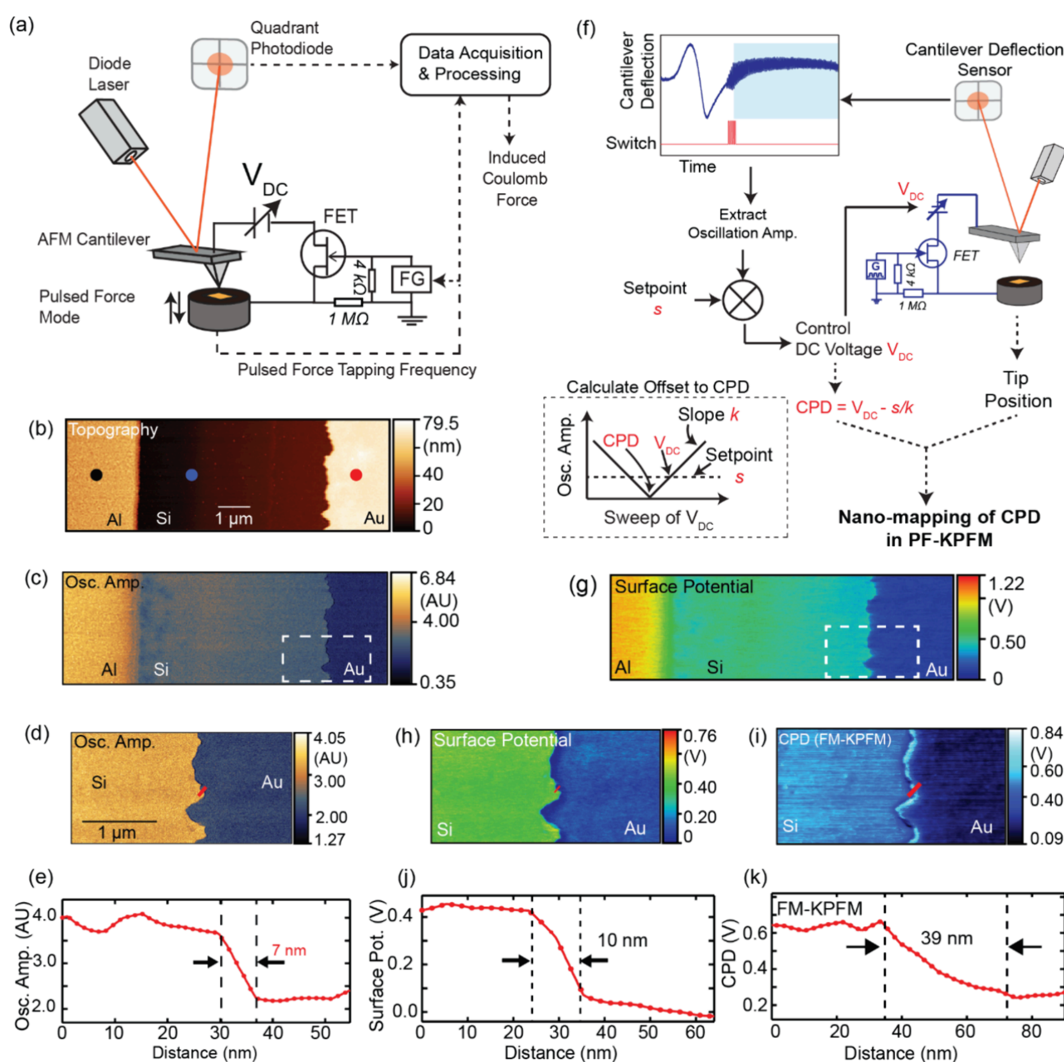

Figure 4. Schematic illustration of open-loop and closed-loop PF-KPFM setup, spatial mapping of cantilever oscillation amplitude, and oscillation amplitude and phase change during V_{DC} sweep on Al/Si/Au sample. A function generator drives FET ON/OFF switching with cantilever free space oscillation frequency, generating Coulombic force oscillation. (a) Schematic connection setup of open-loop PF-KPFM. (b) Topography of the Au/Si/Al sample. (c) Cantilever's Coulombic force-induced oscillation map of the sample. (d) Oscillation amplitude in the Si/Au junction marked with dashed line in panel (c). (e) Oscillation amplitude profile across the red line marked on panel (d). (f) Schematic setup of the closed-loop PF-KPFM and true CPD derivation by offsetting the recorded V_{DC} values from the feedback loop by s/k. (g) Surface potential mapping of the Al/Si/Au sample with closed-loop PF-KPFM. Surface potential mapping of Si/Au section of the sample marked with a dashed line on panel (c), (h) with closed-loop PF-KPFM, and (i) FM-KPFM. CPD profile across the red line marked on the panels (h–i). showing (j) 10 nm spatial resolution for PF-KPFM and (k) 39 nm for FM-KPFM. Adapted with permission from ref 37. Copyright 2020 American Chemical Society.

When the FET is switched OFF, it cuts off the electrical connectivity. A side effect of the FET in its OFF state is its residual capacitance, *i.e.*, the intrinsic capacitance between the source and the drain terminals of the FET when the gate is switched off. The residual capacitance of the FET is larger than the tip–sample junction due to the much larger size of the FET compared with the nanoscopic size of the AFM tip. As a result, the charges formed at the tip and sample migrate to the source and drain terminals of the FET, as they have a larger capacitance. The net effect is that the Coulombic force disappears as the charges migrate away from the tip and sample when the FET is switched off (Figure 3b). As an overall process, when the FET state is periodically switched ON/OFF, the Coulombic force also periodically appears and disappears. As a result, the motion of the AFM cantilever can be periodically driven by switching the FET based on the intrinsic work function differences between the tip and sample without an external AC voltage. If the frequency of the FET switching matches or is close to one of the AFM cantilever mechanical resonances, the Coulombic force-induced cantilever oscillations are amplified and easier to detect.[37]

One limitation of the existing KPFM methods is the necessity of lift mode operation. The AFM probe first scans the sample topography during an initial pass, then is lifted to a height of several tens of nanometers and traverses the same scan line with a constant height with respect to the surface features. Lift mode is useful in avoiding unwanted tip–sample contact when an external AC or DC voltage is applied between the tip and sample— thereby preventing unwanted shorting that could damage the tip and/or sample surfaces. The necessity of the lift mode effectively doubles the operational time and increases the tip–sample distance for the KPFM measurement, thus decreasing the signal contributions from the tip apex region.

https://doi.org/10.1021/acs.jpcc.4c01461
J. Phys. Chem. C 2024, 128, 9813−9827

We solve this limitation by utilizing the pulsed force mode.[40] The pulsed force mode and its later improved versions are commercially known as PeakForce Tapping mode by Bruker,[29] HybriD mode by NT-MDT, Wave mode by Nanosurf, etc. In the pulsed force mode, the AFM tip periodically contacts and detaches from the sample surface at a relatively high frequency of several kHz. The detachment moment is mostly deterministic for samples without unusually high adhesions, *i.e.*, a certain moment exists per every cycle when the tip is just detached from the tip. At this moment and shortly after, the tip and the sample are guaranteed to be spatially separated, like the operation in lift mode. At the same time, the tip−sample distance is very small, in the order of 1−2 nm, since the tip just detached from the sample surface. If Fermi level alignment between the tip and sample occurs at this moment, then the main source of the Coulombic force is at the tip apex, which provides a favorable condition for the KFPM measurement for high spatial resolution. The PF-KPFM technique utilizes this defined moment for surface potential measurement (Figure 3c).

At the core of the PF-KPFM measurement is the temporally synchronized periodical switching of the FET, which generates the Coulombic forces required to drive AFM cantilever oscillation at or close to its mechanical resonance. This condition is achieved by the following key elements:

(a) A time trigger that is synchronized with the AFM cantilever motion. Such a time trigger is used to generate a few periodic ON/OFF switching of the FET to cause periodical Fermi level alignment at or close to the AFM cantilever's mechanical resonance frequency.

(b) An appropriate phase delay to place the ON/OFF switching at the exact moment that tip and sample are detached and in close proximity.

The resulting cantilever oscillation is caused by the Coulombic force from the Fermi level alignment at a configuration when the AFM tip is very close to the sample. Due to the lightning-rod effect, the main contribution to the Coulombic force is from the charges at the AFM tip apex and the sample underneath. Therefore, this configuration has an advantage of better spatial resolution than those KPFM variants that require a separated lift mode at tens of nanometers.

In the PF-KPFM, the oscillation amplitude, S, of the AFM cantilever is recovered by Fourier transform or equivalent lock-in detection in real-time as a single value (Figure 3d). In the absence of a DC nullification bias between tip and sample, S is proportional only to the work function difference. By applying a DC bias, this value also becomes dependent on the externally applied DC voltage magnitude between the AFM tip and the sample. Applying a bias voltage between the tip and the sample affects the amount of electron migration needed to achieve Fermi-level alignment, therefore affecting the generated Coulombic force. When the DC voltage equals the CPD between the tip and the sample, the Coulombic force from the charge migrations due to the Fermi level alignment is nullified, and the oscillation amplitude is minimized. As a result, the oscillation amplitude S versus the external DC voltage sweep exhibits a V-shape (Figure 3e). The corresponding DC voltage at the minimal point of the V-shape (*i.e.*, the intersection between the two branches) is equal to the contact potential difference. If the AFM tip is maintained stationary at a specific location of interest and the DC voltage is changed, the voltage at the intersection of the two branches accurately gives the contact potential difference. If we record the oscillation phase of the cantilever versus the DC voltage sweep, we observe a π phase shift across the CPD (Figure 3f), which can be attributed to the Coulombic force gradient and has a similar origin to the phase shift in FM-KPFM discussed in a previous section.

When spatial mapping of contact potential is desired, the PF-KPFM can operate in either an open-loop mode or a closed-loop mode. In the open-loop mode, the oscillation amplitude is recorded as the AFM tip is scanned over the sample surface without the DC nullification bias. A larger CPD correlates to a bigger difference between the Fermi levels of the tip and sample, which results in a greater Coulombic force and a larger cantilever oscillation amplitude; similarly, at lower CPDs, the oscillation amplitude is smaller. Open-loop PF-KPFM is effectively a special type of electric force microscopy (EFM) implemented in the pulsed force mode without the compensation V_{DC}. The open-loop operation of PF-KPFM gives excellent spatial resolution under ambient conditions, and it can be used to reveal the spatial heterogeneity of the surface potential or accumulated surface charges. Figure 4a displays the construction of an open-loop PF-KPFM. Figure 4**b-c** displays an open-loop PF-KPFM measurement on an Al/Si/Au sample, revealing topography and cantilever oscillation amplitude due to Coulombic force, respectively. A spatial resolution of 7 nm is revealed by analyzing the signal profile across the edge of Si and Au (Figure 4**d-e**).

A more informational implementation of PF-KPFM for imaging is its operation in the closed-loop mode, in which a negative feedback loop is used to dynamically adjust the external DC voltage, similar to typical AM- or FM-KPFM. Figure 4f illustrates the implementation of closed-loop PF-KPFM. The Coulombically driven cantilever oscillation amplitude is used as a real-time process variable; the feedback loop dynamically adjusts the DC voltage between the tip and the sample to regulate the oscillation amplitude at an externally selected set point. However, since the current implementation of PF-KPFM does not use externally applied V_{AC}, when the CPD is fully compensated, the Coulombic force generated oscillation amplitude will be at zero, which is not suitable for a feedback loop to operate at. Therefore, the feedback loop of the closed-loop PF-KPFM is feedback at an offset close to the minimal point of the V-shape curve. We use a small nonzero set point at s (shown in the inset of Figure 4f). The feedback loop adjusts the DC voltage between the AFM tip and the sample so that the oscillation amplitude is maintained constant at the set point during imaging. The DC voltage is coregistered with the lateral position of the AFM tip that is scanned over the sample surface. Then, a DC offset is applied to the acquired DC compensation voltage map to derive what would be the CPD. eq 9 shows the formula to apply the compensation (offset):

$$V_{CPD} \approx V_{DC} - \frac{\boldsymbol{s}}{\boldsymbol{k}} \tag{9}$$

In this expression, the slope k is derived from a V-shape sweep at a location of interest, as seen in Figure 3e. Here, the underlying assumption is that the capacitance gradient term $\frac{\partial C(z)}{\partial z}$ in eqs 2 and 8 do not change their value significantly for relatively flat samples. After applying this offset, the V_{DC} map is then converted into the CPD map. Closed-loop CPD imaging

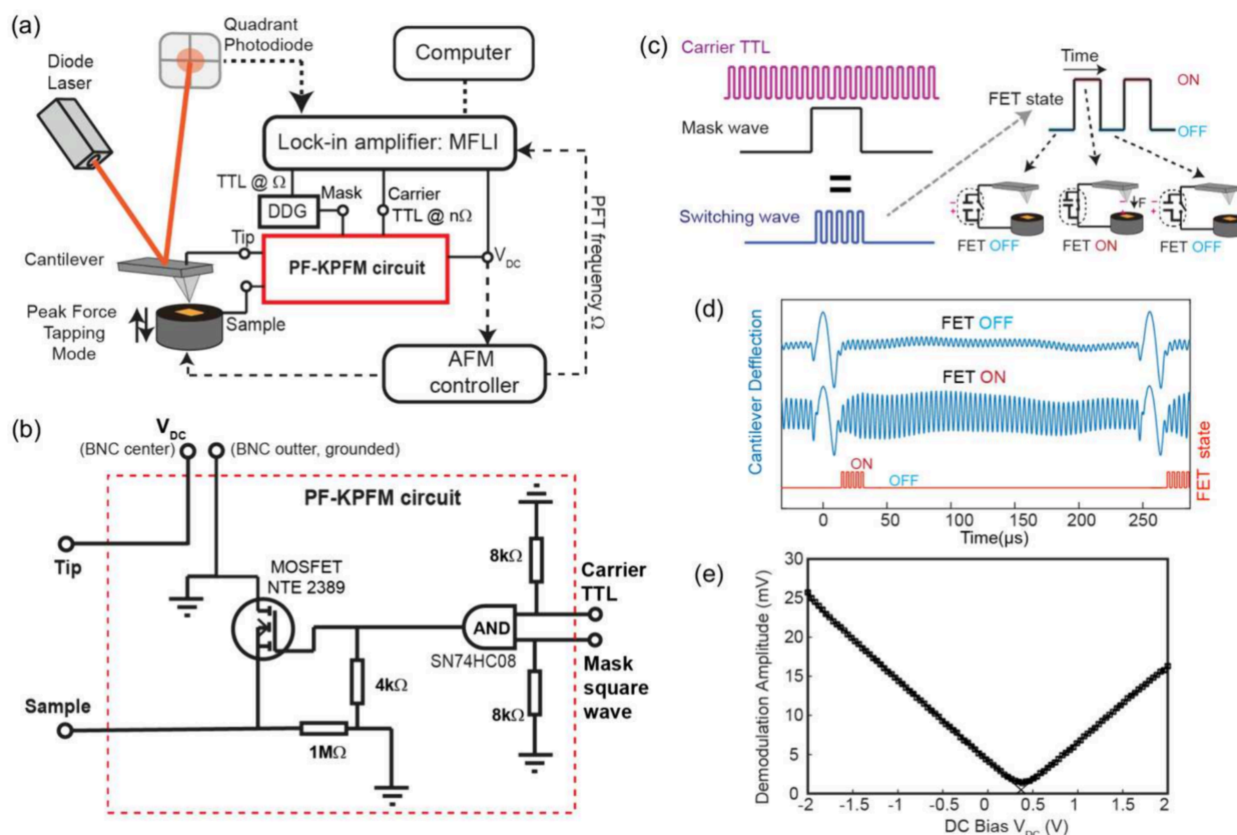

Figure 5. (a) Schematic illustration of the lock-in-based closed-loop PF-KPFM. (b) The custom-made circuit diagram of the lock-in-based PF-KPFM. (c) Illustration of the carrier wave, the mask wave, and the result of masking the carrier TTL wave with AND logic to form a defined switching cluster for switching FET ON and OFF. (d) Coulombic force induced cantilever oscillation in the cantilever vertical deflection curve due to switching the FET ON and OFF (the FET switching cluster is shown in red). (e) Change the demodulation amplitude of the signal as the lock-in sweeps DC bias with a fitted trendline on each branch to find the intersection. Reprinted with permission from ref 41. Copyright 2023 American Chemical Society.

of the Al/Si/Au sample is shown in Figure 4g. Comparing the PF-KPFM to FM-KPFM measurements of the same area of the sample under the same conditions shows that the image obtained with PF-KPFM (Figure 4h) contains significantly reduced noise and an absence of lateral streaks than that with FM-KPFM (Figure 4i), while the CPD spatial profile across the Si/Au section revealed the spatial resolution of 10 nm for PF-KPFM (Figure 4j) as opposed to 39 nm from the commercially available FM-KPFM (Figure 4k).

■ LOCK-IN INTEGRATED PF-KPFM

After the development of digitizer-based PF-KPFM, we further improved the PF-KPFM to increase its operational speed and reduce its complexity. Our first prototype uses a custom-written LabVIEW program to perform data acquisitions and signal processing with a hardware feedback loop. The implementation is difficult to reproduce for those who do not have experience in programming. In an effort to decrease the entry barrier of PF-KPFM and further facilitate its adoption, we have developed a lock-in-based PF-KPFM that has the same complexity as the AM-KPFM.[41]

Tapping mode AFM is used in the regular AM- or FM-KPFM, meaning the cantilever oscillations persist at all times and are thus suitable for lock-in detection. However, for the digitizer-based PF-KPFM, the Coulombic force-induced oscillations are segmented between each tip−sample contact moment during the pulsed force mode AFM operation. The phase of these oscillations lacks a predictable relationship for different tip−sample detachment segments. If these oscillation segments are excited independently of each other, there is no guarantee that they will be constructively added during the lock-in detection. Therefore, we must ensure that the Coulombic force-induced oscillations are in phase for different tip−sample detachment segments so the phase-sensitive lock-in detection will lead to the accurate oscillation amplitude rather than cancellation due to random phase. The above consideration leads us to design a scheme to periodically switch the ON/OFF state of the FET in-phase.

Figure 5 and 5b illustrate a schematic and an electrical circuit design of the lock-in-based PF-KPFM. A lock-in amplifier generates a transistor-transistor logic (TTL) waveform (*i.e.*, a carrier waveform). This carrier waveform is passed to the circuit together with a square-wave mask to generate a cluster of TTL square waves that are temporally synchronized to the moment right after tip−sample detachment (Figure 5c). The periodical switching of the FET causes electrons to migrate between the tip and sample, thereby periodically generating the Coulombic force at the tip apex. Because the FET switching is triggered from the TTL of the carrier waveform, the resulting cantilever oscillations are guaranteed to be in-phase across different tip−sample segments (Figure 5d). This condition is favorable for lock-in detections. The demodulation amplitude from the lock-in detection on the cantilever vertical deflection signal at the carrier TTL

https://doi.org/10.1021/acs.jpcc.4c01461
J. Phys. Chem. C 2024, 128, 9813−9827

frequency will provide the signal as the real-time process variable to the PID feedback loop of the PF-KPFM.

Another advantage of using lock-in detection to recover the oscillation amplitude is that the same signal can be internally routed to the PID controller of the lock-in amplifier, thus avoiding the additional back-and-forth digital to analog conversions and decreasing experimental complexity. The PID adjusts the DC voltage so that the lock-in detected oscillation amplitude is regulated to be the external set point in a similar fashion to the regular PF-KPFM described in the previous sections. The V-shaped sweep (Figure 5e) can also be obtained by sweeping the DC voltage and recording the amplitude of the lock-in demodulation.

EXPERIMENTAL IMPLEMENTATION OF PF-KPFM

PF-KPFM Apparatus Based on a Data Acquisition Card. The setup includes an AFM operating in PFT mode with a line scan of 0.2 Hz (Multimode 8 and Nanoscope V, Bruker); a PeakForce TUNA tip holder (MMCHAM, Bruker); a lock-in amplifier featuring a built-in negative feedback loop (HF2LI with PID, Zurich Instruments); and a voltage-gated circuit regulated by a field-effect transistor (J109, Fairchild). All the electrical connections are made via low-resistance BNC cables to a simple breadboard housing the FET, a 4kΩ and a 4 MΩ resistors for grounding (see Figure 4a).[37] The drain terminal of FET is connected to the TUNA probe holder via a conductive wire, and the source terminal is connected to a jumper of the AFM base, which connects the sample holder of the AFM piezo scanner. To establish an electrical connection between the sample surface and the AFM sample holder, all samples were glued to regular conductive AFM specimen disks (Ted Pella) and then electrically connected to the disk with adhesive copper tape or silver paint (Leitsilber 200 silver paint, Ted Pella).[37,41]

A platinum-coated AFM cantilever (HQ:NSC15/Pt, Mikro-Masch) is used. In pulsed force or peak force tapping mode, the sample stage performs a sinusoidal *z*-axis motion at a predefined frequency (1.975 kHz) which is far lower than the cantilever free space resonance frequency (∼250 to 300 kHz for HQ:NSC15/Pt, Mikromasch). This motion causes tip and sample physical attachment in a range of a few microseconds. A phase-locked loop locked at the frequency of PFT is used to trigger a function generator (2022B, Hantek) with a tunable phase delay. By adjusting to an appropriate phase delay, a set of TTL voltage waveforms between −5 and 0 V with a 50% duty cycle is used to drive the FET gate to position the switching process exactly after the tip and sample detachment to ensure the proximity of the tip apex and sample surface.[37]

The AFM cantilever oscillations are directed to a data acquisition card (DAC) (PXI-5122, National Instrument). The locked PFT frequency from the lock-in is used to trigger the DAC. By using the fast-Fourier transform (FFT), the Coulombic force oscillations (Figure 3c) translate from the time domain to the frequency domain, and the signal peak appears at the cantilever's free space resonance oscillation frequency (Figure 3d). Integration of the surface area under the peak represents the magnitude of the signal which directly correlates to CPD.[37]

A negative feedback loop (HF2LI-PID Zurich Instrument) constantly applies the appropriate external DC potential between tip and sample to keep the signal (peak surface area) constant on an externally defined set point. True CPD can then be easily derived by offsetting the data using the slope of the signal versus the V_{DC} plot (Figure 3e and 4f) according to eq 9.[37]

Lock-In Integrated PF-KPFM. The layout of the lock-in-based PF-KPFM setup is shown in Figure 5a, which consists of three primary components: Peak Force Tapping enabled atomic force microscope (AFM) unit (Multimode 8 by Bruker), a custom-designed PF-KPFM triggering circuit (Figure 5b), and a lock-in amplifier (MFLI-MD-PID by Zurich Instruments). In operation, the AFM operates at a PFT frequency of 3.952 kHz and utilizes a conductive Pt-coated probe with a spring constant of approximately 40 N/m (HQ:NSC15/Pt MikroMasch) to achieve a peak force amplitude of 30 nm.[41]

The AFM controller used in lock-in-based PF-KPFM works in the pulsed force mode/peak force tapping mode. The driving voltage waveform of the pulsed force mode is routed from the AFM controller to the lock-in amplifier to generate a synchronized TTL waveform at a frequency denoted as Ω (PFT frequency *i.e.*, 3.95 kHz). This TTL waveform serves as the trigger for a digital delay generator (DG645, SRS), allowing the creation of an adjustable square wave mask with voltage levels of 0 V and +5 V, and it permits the adjustment of both delay and duration. The timing of this mask is carefully chosen to coincide with the moment immediately after the tip detaches from the sample during each PFT cycle. The lock-in amplifier also produces a carrier TTL waveform at an integer multiple of the PFT frequency, determined by configuring the demodulation harmonic to the nth order (nΩ). The choice of integer 'n' ensures that nΩ is close to the free space cantilever's resonant oscillation frequency. This same harmonic frequency, nΩ, serves as the reference frequency for the lock-in demodulation. The square masking waveform and carrier TTL waveform are then directed into the custom-built PF-KPFM circuit (Figure 5b). In the circuit, the carrier TTL and the square wave mask are combined at the inputs of the AND logic gate (CD4081BE), producing a set of square wave signals. These square waves occur at a frequency of nΩ during a short period of time (defined by mask waveform duration), immediately after the AFM tip is just detached from the sample, maintaining a separation of a few nanometers. The output from the AND logic gate is connected to the gate terminal of a FET (NTE2389). The cluster of square waves applied to the FET periodically toggles the electrical connectivity between the source and the drain, switching it ON and OFF.[41] The cantilever's vertical deflection waveform is routed to the lock-in amplifier that extracts both the amplitude and phase of the cantilever's oscillations due to Coulombic force. A lock-in time constant of 1.5 ms, covering around 6 PFT cycles (approximately 250 μs for each cycle), is employed. This setup enables PF-KPFM operation up to 0.8 Hz per AFM scan line,[41] which is almost 1 order of magnitude faster than that of FM-KPFM.

The cantilever oscillation amplitude is internally routed by the multifunction lock-in amplifier (MFLI-MD-PID) to its proportional-integral-derivative (PID) negative feedback loop functionality, which operates in PI mode. The analog V_{DC} from the lock-in amplifier output is applied to the tip to maintain the demodulation amplitude on the set point value and coregistered by the AFM controller as the tip scans.[41]

Accurate CPD values from individual positions are obtained by sweeping the external bias voltage V_{DC} and registering the amplitude of the Coulombic force-induced cantilever oscillations from the lock-in demodulation (Figure 5e). The CPD

https://doi.org/10.1021/acs.jpcc.4c01461
J. Phys. Chem. C 2024, 128, 9813−9827

value of the sample surface is determined by the intersection between the two branches of the V-shape pattern. In the lock-in-based PF-KPFM, the collection of the V-shape sweeping is achieved with the built-in parameter sweeping functionality of the lock-in amplifier, *i.e.*, sweeping the analog output that is connected to V_{DC} within a range and registering the lock-in demodulation.[41] Unlike the original LabVIEW-based PF-KPFM, such a sweeping operation does not require additional programming or a data acquisition card.[37,42]

■ APPLICATIONS OF PF-KPFM

Revealing the Surface Accumulated Charges. Besides the measurement of surface work function, another application of KPFM is to reveal the surface accumulated charges. The locally accumulated charges can be the result of the carrier's presence on the surface. KPFM, being an electrical scanning probe microscopy, can detect the presence of surface accumulated charges. This ability also applies to the PF-KPFM. Figure 6**a**-**b** show the topography and surface potential image for crystalline $MAPbBr_3$ (methylammonium lead tribromide) perovskite. $MAPbBr_3$ crystals can undergo decomposition in the presence of humidity and at high temperatures with the following reaction:

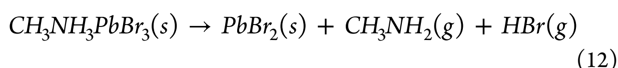

$$CH_3NH_3PbBr_3(s) \rightarrow PbBr_2(s) + CH_3NH_2(g) + HBr(g) \quad (12)$$

Here, perovskite crystals were degraded by a sudden increase in temperature using a pulsed IR laser and partially cleaved (left). Growth and new boundary formation of degraded crystals are shown in Figure 6a (right). The PF-KPFM image revealed charge accumulations at the interface of the freshly cleaved perovskite with degraded grown crystals.[42]

Early-Stage Identification of Degradations in Photovoltaic Perovskites. Mixed halide perovskites (MHPs) are another family of perovskites with photovoltaic applications.[43] The photovoltaic properties and efficiency of MHPs, however, are highly dependent on their stability.[44] These perovskites can degrade in the presence of light,[44] humidity,[45] at high temperatures,[46] and also endure halide exchange[47] or ion migration[48] which results in a reduction in the efficiency and instability of these materials.[44] However, detecting the initial phase of these degradations could be highly beneficial to achieve preventive and remedial measures. The topography of an aged thin film $Cs_{0.05}(FA_{0.93}MA_{0.07})_{0.95}PbI_3$ perovskite is shown in Figure 6c. Initial topographic assessment of the film does not indicate any sign of degradation, but CPD mapping of the same area (Figure 6**d**) with lock-in based PF-KPFM reveals an electrical state degradation which would have been impossible to detect with common topological analysis using regular AFM,[41] or KPFMs with insufficient spatial resolution.

Surface Potential Study of 2D Materials. MXenes are a family of two-dimensional (2D) materials with extraordinary electrical, optical, and mechanical properties, which have great potential in energy storage and harvesting, catalysis, electronics, and optics applications.[49] As 2D materials with thicknesses that may not exceed a few nanometers and lateral features of 2D material devices are on the order of a few hundred nanometers, the nanoscale measurement of surface potential can be challenging. The PF-KPFM is capable of such measurement. Figure 6**e**-**f** show the topography and CPD of a multilayer $Ti_3C_2T_x$ MXene flake on a Si substrate. Despite the small thicknesses of the flakes, the PF-KPFM method identifies the CPD value for different stacked MXene flakes of varying thicknesses (5−15 nm). Further analysis of the CPD values of different thicknesses revealed that 1 layer flake of MXene with approximately 8 nm in thickness has a CPD value closer to the Si substrate while all 2, 3, 4, and 5 layered stacks pose similar CPD, indicating full electrical shielding of the substrate cannot be achieved with 1 layer flake with 8 nm thickness.[41]

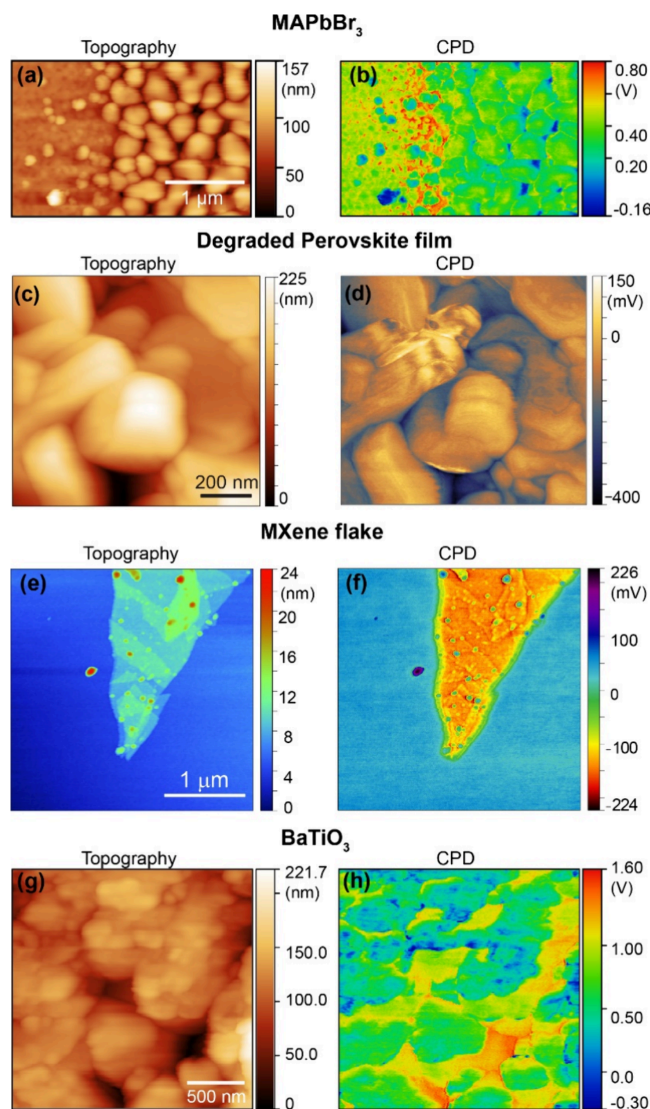

Figure 6. PF-KPFM CPD mapping of different samples along their topography channels. (a) Topography and (b) CPD mapping showing charge accumulation around degradation boundaries in $MAPbBr_3$ perovskite crystals. (c, d) Electrical state degradation was revealed on the surface of $Cs_{0.05}(FA_{0.93}MA_{0.07})_{0.95}PbI_3$ perovskite thin film, which is undetectable in the topography channel. (e, f) CPD mapping of the Ti_3C_2Tx MXene flakes on top of a silicon wafer. (g, h) Revealing the anisotropic ferroelectric behavior of barium titanate. CPD mapping of $BaTiO_3$ showed different surface potentials for grains with the same topography, indicating different unit cell elongation directions. Panels (a-b) adapted with permission from ref 42. Copyright 2020 Wiley-VCH Verlag GmbH & Co. KGaA, Weinheim. Panels (c−f) adapted with permission from ref 41. Copyright 2023 American Chemical Society. Panels (g, h) adapted with permission from ref 37. Copyright 2020 American Chemical Society.

Anisotropic Ferroelectric Behavior of $BaTiO_3$. Barium titanate ($BaTiO_3$) and other ferroelectric oxides exhibit spontaneous polarization below the Curie temperature,

resulting in the formation of anisotropic ferroelectric domains.[50] These domains are capable of reorienting under an electric field, which resulted in various applications for them in memory storage devices,[51] microelectromechanical sensors and actuators,[52] medical ultrasound imaging devices,[53] and signal processing for optical communication systems.[54] Research on the specific properties of local ferroelectric domains within ferroelectric materials is crucial for enhancing their performance and functionality. PF-KPFM provides sufficient spatial resolution to study these materials in greater detail. The topography and surface potential mapping of the $BaTiO_3$ are shown in Figure 6**g-h**. The difference in surface potential for grains with the same topography reveals different polarization of crystals alongside different unit cell elongation directions.[37]

Revealing the Band Bending at Material Interfaces at Nanometric Scales. When materials of different Fermi levels come in contact with each other, electrons flow from the material with a low Fermi level to the material with a high Fermi level, leaving positive charges behind. Such a migration forms a space charge layer on a nanometric scale between the two materials. The electrical field of the spatial charge layer prevents further electron migration and aligns the Fermi levels of the two materials by shifting the band positions, also known as band bending. The formation of the spatial charge layer is a fundamental phenomenon for the properties of semiconductors.

One characteristic of the spatial charge layer is that it shifts the local surface electrical potential, which can be measured by KPFM. On the other hand, the spatial scale of the band bending is relatively short, which is often smaller than the typical spatial resolution of commercially available KPFMs under ambient conditions. The development of PF-KPFM with improved spatial resolution enables the opportunity to study this phenomenon.[37]

Figure 7 displays the measurement of CPD at the interfaces between Al and Si, as well as between Si and Au obtained with PF-KPFM. The contacts between metal and semiconductors are typically either an ohmic contact or a Schottky contact. Electrons can usually move across an ohmic contact without significant voltage drop. In the case of Schottky contact, a voltage barrier exists, and electrons cannot move freely in both directions. At the nanoscale, an experimental tool for *in situ* evaluation is needed to determine which type of contact is between metal and semiconductor. With the high spatial resolution of PF-KPFM, we identify that our sample's contact between Al and Si is ohmic, as the surface potential gradually changes across the Si/Al interface. On the other hand, the contact between Au/Si is Schottky, as a discontinuity exists and a clear step-like change of surface potential is observed.[37]

Limitation and Outlook for PF-KPFM. The PF-KPFM, although delivering significantly better spatial resolution and operational speed than the FM-KPFM under ambient conditions, still has challenges and limitations. One limitation is that the PF-KPFM in the imaging mode only partially compensates for the CPD. An afterward correction is needed. When the sample topography has a large variation, the capacitance gradient term would be spatially nonuniform, a uniform correction value like in eq 9 would lead to potential errors. The V-shape curve of PF-KPFM in the spectroscopy mode yields highly accurate CPD, however, it is only a point measurement. A possible remedy for this limitation is to consider the topography information and employ postprocessing to evaluate the spatial variation in the capacitance gradient numerically. For example, one could perform a finite element simulation to calculate the capacitance between a sample with experimentally measured topography and an apex of the metallic tip of the KPFM measurement. Such a simulation would derive the spatial variation of the capacitance gradient for a more accurate correction term. Another possibility for improvement of PF-KPFM is to implement a machine learning technique that deals with spare sampling. For example, a compressed sensing algorithm may combine several dozens of V-shape spectroscopy measurements, a partially compensated PF-KPFM image, and topography to reconstruct an accurate CPD map with both high accuracy and spatial resolution.

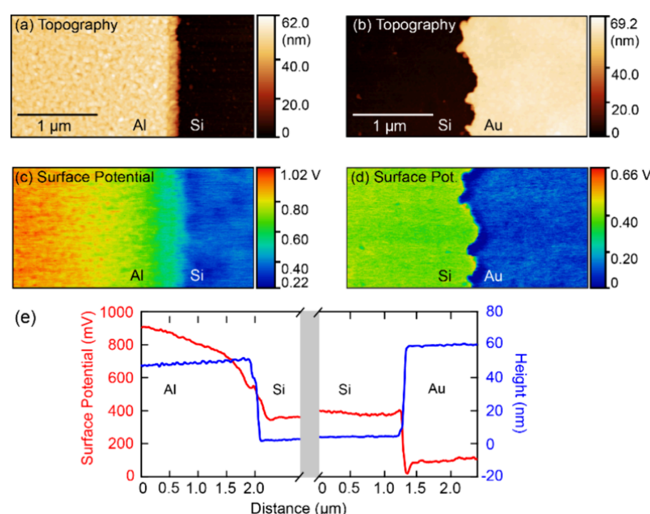

Figure 7. PF-KPFM CPD mapping and surface potential bending at interfaces. Topography of (a) Al/Si and (b) Si/Au interface. CPD mapping of (c) Al/Si and (d) Si/Au interface. (e) Surface potential spatial profile across the interfaces. The gradual surface potential change between the Al/Si interface shows an ohmic contact between them, whereas the step-like change of the potential across the Si/Au exhibits a Schottky contact. Adapted with permission from ref 37. Copyright 2020 American Chemical Society.

Challenges of KPFM as a General Nanoelectrical Characterization Tool for Chemistry Applications. A common challenge to all variants of KPFMs under ambient conditions is the interpretation of the measured surface potential values. In conductive or semiconductive samples, such as pure metals, alloys, and doped silicon, the main contribution to the surface potential is the CPD between the sample and the metallic tip, which originates from the work functions or Fermi levels. In the case of the surface accumulation of charges in the insulator, the surface potential is not from the CPD between the materials but rather the electric potential of the sample due to the presence of these charge polarization. However, when samples are more complex, for example, metal on metal-oxide heterostructures, the interpretation of the surface potential becomes more complicated. On the other hand, metal and metal oxide heterostructures are commonly used in heterogeneous catalysis. Their sizes are usually small, and the information on band positions is important to decipher the catalytic activities. However, the existing capacitor model (eq 2) would not give a clear interpretation of these heterostructures. Interpretation of spatially resolved measurement from such

heterostructures may be assisted by finite element methods, such as COMSOL.

Another challenge of KPFM is the treatment of surface contaminations. For example, organic molecules may be present on a metallic surface (*e.g.*, thiols on a gold surface). How would the thin layer of an organic molecule affect the surface potential? So far, this situation is treated as nuances or situations to be avoided. On the other hand, given that the current experimental tools, such as the nano-IRs,[42,55,56] can identify surface contamination, computational tools are sophisticated enough to reveal detailed electronic structures and polarizability of the organic molecules. It should be possible to account for the surface contamination during a KPFM measurement to reveal the true Fermi levels of the sample. However, this capability has yet to be realized and remains to be explored by the joint efforts between experimentalists and theorists.

Outlook of the Applications of KPFM. As an available tool for chemical studies, KPFM, in general, provides a versatile tool for probing and understanding various aspects of material properties and behaviors at the nanoscale. One significant application is in surface potential mapping, where KPFM allows for precise delineation of surface potential variations, essential for deciphering surface charge distribution and electronic properties in semiconductor devices, catalysis, and energy materials,[57−62] as well as the emergence of charges due to frictions—through triboelectric charging.[63] KPFM can also reveal surface modifications and provide insights into how surface alterations impact the electronic properties of materials, which is useful in the design of electronic devices, sensors, and catalysts.[64,65] Additionally, when coupled with electrochemical techniques, KPFM would enable the investigation of the transformation of electrode surfaces,[66,67] shedding light on the processes of degradation and modifications of the electrodes in batteries. In the realm of nanoelectronics and device characterization, KPFM contributes to understanding the local electrical properties of nanostructured materials, which is essential for optimizing device performance based on 2D materials.[68,69] Lastly, in corrosion and surface degradation studies, KPFM, with fast operational speed, is an effective tool for monitoring surface potential changes over time. It offers valuable insights into corrosion processes and localized degradation phenomena, thereby aiding in the development of effective corrosion protection strategies.[70] With the spatial resolution of PF-KPFM reaching <10 nm under ambient conditions, these above areas of research shall be facilitated for new discoveries.

AUTHOR INFORMATION

Corresponding Author

Xiaoji G. Xu − *Department of Chemistry, Lehigh University, Bethlehem, Pennsylvania 18015, United States*; orcid.org/0000-0003-0847-5871; Email: xgx214@lehigh.edu

Authors

Amirhossein Zahmatkeshsaredorahi − *Department of Chemistry, Lehigh University, Bethlehem, Pennsylvania 18015, United States*

Devon S. Jakob − *Department of Chemistry, Lehigh University, Bethlehem, Pennsylvania 18015, United States*; orcid.org/0000-0002-6534-4803

Complete contact information is available at: https://pubs.acs.org/10.1021/acs.jpcc.4c01461

Author Contributions

‡A.Z and D.S.J. contributed equally.

Notes

The authors declare no competing financial interest.

Biographies

Amirhossein Zahmatkeshsaredorahi is currently a chemistry Ph.D. student in Prof. Xiaoji G. Xu's laboratory at Lehigh University, Bethlehem, PA. He graduated from Sharif University of Technology in 2015 with a master's degree in materials science and engineering. His current research aims at the development of new Kelvin probe force microscopy variants with high scan rates and spatial resolution and utilizing them to study semiconductors and 2D materials.

Devon S. Jakob obtained his P.hD. in chemistry at Lehigh University in 2021 under the supervision of Prof. Xiaoji G. Xu. He joined Dr. Andrea Centrone's group at the National Institute of Standards and Technology later the same year through the NIST Professional Research Experience Program with Georgetown University. His expertise is in the development of novel atomic force microscopy techniques for improved spatial resolution and improved imaging capabilities. He is the coinventor of pulsed force Kelvin probe force microscopy (PF-KPFM) and has also worked extensively with several AFM-based chemical mapping techniques such as PFIR, PTIR, and PiFM.

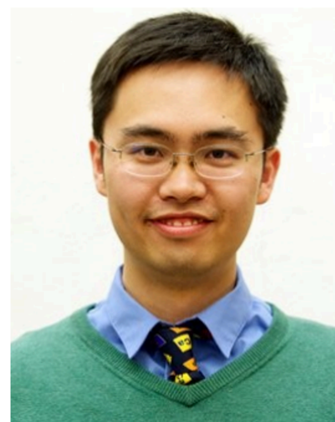

https://doi.org/10.1021/acs.jpcc.4c01461
J. Phys. Chem. C 2024, 128, 9813−9827

Dr. Xiaoji Xu is currently an associate professor in the Department of Chemistry at Lehigh University in Bethlehem, Pennsylvania. Prior to an independent research career, he was a postdoctoral fellow at the University of Toronto with Dr. Gilbert C. Walker. He received his B.S. from Peking University in 2004 and Ph.D. from The University of British Columbia in 2009. His current research focuses are on nanoscale chemical imaging, laser spectroscopy, and innovations in scanning probe microscopy for chemical and electrical measurement, including near-field microscopy, photothermal AFM-IR, and pulsed force KPFM. He has published more than 60 peer-reviewed articles and holds several granted patents on AFM-based infrared microscopy. He was selected as a Beckman Young Investigator in 2018 and Sloan Research Fellow in 2020. He is also a recipient of the Camille Dreyfus Teacher-Scholar Award in 2021.

■ ACKNOWLEDGMENTS

X.G.X., D.S.J., and A.Z. are thankful for the support from the National Science Foundation, award number CHE 1847765, and the Faculty Innovation Grant 2019 from Lehigh University.

■ REFERENCES

(1) Binnig, G.; Quate, C. F.; Gerber, C. Atomic force microscope. *Phys. Rev. Lett.* **1986**, *56* (9), 930.
(2) Cheon, J. Y.; Kim, J. H.; Kim, J. H.; Goddeti, K. C.; Park, J. Y.; Joo, S. H. Intrinsic relationship between enhanced oxygen reduction reaction activity and nanoscale work function of doped carbons. *J. Am. Chem. Soc.* **2014**, *136* (25), 8875−8878.
(3) Choi, S.; Shaolin, Z.; Yang, W. Layer-number-dependent work function of MoS 2 nanoflakes. *J. Am. Chem. Soc.* **2014**, *64*, 1550−1555.
(4) Nonnenmacher, M.; o'Boyle, M.; Wickramasinghe, H. K. Kelvin probe force microscopy. *Appl. Phys. Lett.* **1991**, *58* (25), 2921−2923.
(5) Kikukawa, A.; Hosaka, S.; Imura, R. Silicon pn junction imaging and characterizations using sensitivity enhanced Kelvin probe force microscopy. *Appl. Phys. Lett.* **1995**, *66* (25), 3510−3512.
(6) Shvebelman, M. M.; Agronin, A. G.; Urenski, R. P.; Rosenwaks, Y.; Rosenman, G. I. Kelvin probe force microscopy of periodic ferroelectric domain structure in KTiOPO4 crystals. *Nano Lett.* **2002**, *2* (5), 455−458.
(7) Xiao, Z.; Yuan, Y.; Shao, Y.; Wang, Q.; Dong, Q.; Bi, C.; Sharma, P.; Gruverman, A.; Huang, J. Giant switchable photovoltaic effect in organometal trihalide perovskite devices. *Nat. Mater.* **2015**, *14* (2), 193−198.
(8) Li, N.; Niu, X.; Li, L.; Wang, H.; Huang, Z.; Zhang, Y.; Chen, Y.; Zhang, X.; Zhu, C.; Zai, H.; Bai, Y.; Ma, S.; Liu, H.; Liu, X.; Guo, Z.; Liu, G.; Fan, R.; Chen, H.; Wang, J.; Lun, Y.; Wang, X.; Hong, J.; Xie, H.; Jakob, D. S.; Xu, X. G.; Chen, Q.; Zhou, H. Liquid medium annealing for fabricating durable perovskite solar cells with improved reproducibility. *Science* **2021**, *373* (6554), 561−567.
(9) Ravi, S. K.; Rawding, P.; Elshahawy, A. M.; Huang, K.; Sun, W.; Zhao, F.; Wang, J.; Jones, M. R.; Tan, S. C. Photosynthetic apparatus of Rhodobacter sphaeroides exhibits prolonged charge storage. *Nat. Commun.* **2019**, *10* (1), 902.
(10) Iglesias, V.; Lanza, M.; Zhang, K.; Bayerl, A.; Porti, M.; Nafría, M.; Aymerich, X.; Benstetter, G.; Shen, Z.; Bersuker, G. Degradation of polycrystalline HfO2-based gate dielectrics under nanoscale electrical stress. *Appl. Phys. Lett.* **2011**, *99* (10), 103510.
(11) Tung, R. T. The physics and chemistry of the Schottky barrier height. *Applied Physics Reviews* **2014**, *1* (1), 011304.
(12) Rohwerder, M.; Turcu, F. High-resolution Kelvin probe microscopy in corrosion science: scanning Kelvin probe force microscopy (SKPFM) versus classical scanning Kelvin probe (SKP). *Electrochim. Acta* **2007**, *53* (2), 290−299.
(13) Lägel, B.; Baikie, I.; Petermann, U. A novel detection system for defects and chemical contamination in semiconductors based upon the Scanning Kelvin Probe. *Surf. Sci.* **1999**, *433*, 622−626.
(14) Sadewasser, S.; Glatzel, T.; Rusu, M.; Jäger-Waldau, A.; Lux-Steiner, M. C. High-resolution work function imaging of single grains of semiconductor surfaces. *Appl. Phys. Lett.* **2002**, *80* (16), 2979−2981.
(15) Ma, J.-Y.; Ding, J.; Yan, H.-J.; Wang, D.; Hu, J.-S. interfaces. Temperature-dependent local electrical properties of organic−inorganic halide perovskites: in situ KPFM and c-AFM investigation. *ACS Applied Materials* **2019**, *11* (24), 21627−21633.
(16) Kelvin, L. V. Contact electricity of metals. *London, Edinburgh, Dublin Philosophical Magazine, Journal of Science* **1898**, *46* (278), 82−120.
(17) Shockley, W.; Hooper, W.; Queisser, H.; Schroen, W. Mobile electric charges on insulating oxides with application to oxide covered silicon pn junctions. *Surf. Sci.* **1964**, *2*, 277−287.
(18) Alexander, S.; Hellemans, L.; Marti, O.; Schneir, J.; Elings, V.; Hansma, P. K.; Longmire, M.; Gurley, J. An atomic-resolution atomic-force microscope implemented using an optical lever. *J. Appl. Phys.* **1989**, *65* (1), 164−167.
(19) Girard, P. Electrostatic force microscopy: principles and some applications to semiconductors. *Nanotechnology* **2001**, *12* (4), 485.
(20) Kitamura, S. i.; Iwatsuki, M. High-resolution imaging of contact potential difference with ultrahigh vacuum noncontact atomic force microscope. *Appl. Phys. Lett.* **1998**, *72* (24), 3154−3156.
(21) Gruverman, A.; Alexe, M.; Meier, D. Piezoresponse force microscopy and nanoferroic phenomena. *Nat. Commun.* **2019**, *10* (1), 1661.
(22) Kalinin, S. V.; Rar, A.; Jesse, S. A decade of piezoresponse force microscopy: progress, challenges, and opportunities. *IEEE transactions on ultrasonics, ferroelectrics, and frequency control* **2006**, *53* (12), 2226−2252.
(23) Colchero, J.; Gil, A.; Baró, A. Resolution enhancement and improved data interpretation in electrostatic force microscopy. *Phys. Rev. B* **2001**, *64* (24), No. 245403.
(24) Jacobs, H. O.; Knapp, H. F.; Müller, S.; Stemmer, A. Surface potential mapping: A qualitative material contrast in SPM. *Ultramicroscopy* **1997**, *69* (1), 39−49.
(25) Koley, G.; Spencer, M. G.; Bhangale, H. R. Cantilever effects on the measurement of electrostatic potentials by scanning Kelvin probe microscopy. *Appl. Phys. Lett.* **2001**, *79* (4), 545−547.
(26) Ma, Z. M.; Kou, L.; Naitoh, Y.; Li, Y. J.; Sugawara, Y. The stray capacitance effect in Kelvin probe force microscopy using FM, AM and heterodyne AM modes. *Nanotechnology* **2013**, *24* (22), No. 225701.
(27) Zerweck, U.; Loppacher, C.; Otto, T.; Grafström, S.; Eng, L. M. Accuracy and resolution limits of Kelvin probe force microscopy. *Phys. Rev. B* **2005**, *71* (12), No. 125424.
(28) Ziegler, D.; Stemmer, A. Force gradient sensitive detection in lift-mode Kelvin probe force microscopy. *Nanotechnology* **2011**, *22* (7), No. 075501.
(29) Pittenger, B.; Erina, N.; Su, C.*Quantitative mechanical property mapping at the nanoscale with PeakForce QNM*; Application Note; Veeco Instruments, Inc, 2010. DOI: 10.13140/RG.2.1.4463.8246.
(30) Krok, F.; Sajewicz, K.; Konior, J.; Goryl, M.; Piatkowski, P.; Szymonski, M. Lateral resolution and potential sensitivity in Kelvin probe force microscopy: Towards understanding of the sub-nanometer resolution. *Phys. Rev. B* **2008**, *77* (23), No. 235427.
(31) Kitamura, S. i.; Suzuki, K.; Iwatsuki, M.; Mooney, C. B. Atomic-scale variations in contact potential difference on Au/Si(111) 7 × 7 surface in ultrahigh vacuum. *Appl. Surf. Sci.* **2000**, *157* (4), 222−227.
(32) Bahrami, A.; Nayfeh, A. H. Nonlinear dynamics of tapping mode atomic force microscopy in the bistable phase. *Communications in Nonlinear Science and Numerical Simulation* **2013**, *18* (3), 799−810.
(33) Santos, S.; Barcons, V.; Font, J.; Thomson, N. H. Bi-stability of amplitude modulation AFM in air: deterministic and stochastic outcomes for imaging biomolecular systems. *Nanotechnology* **2010**, *21* (22), No. 225710.

(34) Stan, G.; Namboodiri, P. Open-loop amplitude-modulation Kelvin probe force microscopy operated in single-pass PeakForce tapping mode. *Beilstein Journal of Nanotechnology* **2021**, *12*, 1115−1126.
(35) Sugawara, Y.; Kou, L.; Ma, Z.; Kamijo, T.; Naitoh, Y.; Jun Li, Y. High potential sensitivity in heterodyne amplitude-modulation Kelvin probe force microscopy. *Appl. Phys. Lett.* **2012**, *100* (22), No. 223104.
(36) Garrett, J. L.; Munday, J. N. Fast, high-resolution surface potential measurements in air with heterodyne Kelvin probe force microscopy. *Nanotechnology* **2016**, *27* (24), No. 245705.
(37) Jakob, D. S.; Wang, H.; Xu, X. G. Pulsed force Kelvin probe force microscopy. *ACS Nano* **2020**, *14* (4), 4839−4848.
(38) Kelvin, L. V. Contact electricity of metals. *London, Edinburgh, and Dublin Philosophical Magazine and Journal of Science* **1898**, *46* (278), 82−120.
(39) Baikie, I. D.; Estrup, P. J. Low cost PC based scanning Kelvin probe. *Rev. Sci. Instrum.* **1998**, *69* (11), 3902−3907.
(40) Krotil, H. U.; Stifter, T.; Waschipky, H.; Weishaupt, K.; Hild, S.; Marti, O. Pulsed force mode: a new method for the investigation of surface properties. *Surf. Interface Anal.* **1999**, *27* (5−6), 336−340.
(41) Zahmatkeshsaredorahi, A.; Jakob, D. S.; Fang, H.; Fakhraai, Z.; Xu, X. G. Pulsed Force Kelvin Probe Force Microscopy through Integration of Lock-In Detection. *Nano Lett.* **2023**, *23* (19), 8953−8959.
(42) Jakob, D. S.; Wang, H.; Zeng, G.; Otzen, D. E.; Yan, Y.; Xu, X. G. Peak force infrared−kelvin probe force microscopy. *Angewandte Chemie Int. Ed.* **2020**, *132* (37), 16217−16224.
(43) Choe, H.; Jeon, D.; Lee, S. J.; Cho, J. Mixed or segregated: Toward efficient and stable mixed halide perovskite-based devices. *ACS Omega* **2021**, *6* (38), 24304−24315.
(44) Mao, W.; Hall, C. R.; Bernardi, S.; Cheng, Y.-B.; Widmer-Cooper, A.; Smith, T. A.; Bach, U. Light-induced reversal of ion segregation in mixed-halide perovskites. *Nat. Mater.* **2021**, *20* (1), 55−61.
(45) Yao, W.; Ling, Q.; Dai, Q.; Fang, S.; Yang, C.; Huang, L.; Liu, X.; Zhang, H.; Zhang, J.; Zhu, Y.; Hu, Z. In Situ Microscopic Observation of Humidity-Induced Degradation in All-Inorganic Perovskite Films. *ACS Applied Energy Materials* **2022**, *5* (7), 8092−8102.
(46) Yang, J.; Siempelkamp, B. D.; Mosconi, E.; De Angelis, F.; Kelly, T. L. Origin of the thermal instability in CH3NH3PbI3 thin films deposited on ZnO. *Chem. Mater.* **2015**, *27* (12), 4229−4236.
(47) Noh, J. H.; Im, S. H.; Heo, J. H.; Mandal, T. N.; Seok, S. I. Chemical management for colorful, efficient, and stable inorganic−organic hybrid nanostructured solar cells. *Nano Lett.* **2013**, *13* (4), 1764−1769.
(48) Yang, S.; Fu, W.; Zhang, Z.; Chen, H.; Li, C.-Z. Recent advances in perovskite solar cells: efficiency, stability and lead-free perovskite. *Journal of Materials Chemistry A* **2017**, *5* (23), 11462−11482.
(49) Anasori, B.; Lukatskaya, M. R.; Gogotsi, Y. 2D metal carbides and nitrides (MXenes) for energy storage. *Nature Reviews Materials* **2017**, *2* (2), 1−17.
(50) Chen, X.; Yamada, H.; Horiuchi, T.; Matsushige, K.; Watanabe, S.; Kawai, M.; Weiss, P. Surface potential of ferroelectric thin films investigated by scanning probe microscopy. *Journal of Vacuum Science Technology B: Microelectronics Nanometer Structures Processing, Measurement, Phenomena* **1999**, *17* (5), 1930−1934.
(51) Trolier-McKinstry, S.; Muralt, P. Thin film piezoelectrics for MEMS. *Journal of Electroceramics* **2004**, *12*, 7−17.
(52) Aksel, E.; Jones, J. L. Advances in lead-free piezoelectric materials for sensors and actuators. *Sensors* **2010**, *10* (3), 1935−1954.
(53) Gallego-Juarez, J. Piezoelectric ceramics and ultrasonic transducers. *Journal of Physics E: Scientific Instruments* **1989**, *22* (10), 804.
(54) Tang, P.; Towner, D.; Hamano, T.; Meier, A.; Wessels, B. Electrooptic modulation up to 40 GHz in a barium titanate thin film waveguide modulator. *Opt. Express* **2004**, *12* (24), 5962−5967.
(55) Mathurin, J.; Deniset-Besseau, A.; Bazin, D.; Dartois, E.; Wagner, M.; Dazzi, A. Photothermal AFM-IR spectroscopy and imaging: Status, challenges, and trends. *J. Appl. Phys.* **2022**, *131* (1), 010901.
(56) Wang, H.; Xie, Q.; Xu, X. G. Super-resolution mid-infrared spectro-microscopy of biological applications through tapping mode and peak force tapping mode atomic force microscope. *Adv. Drug Delivery Rev.* **2022**, *180*, No. 114080.
(57) Tran, H. P.; Nong, H. N.; Oh, H.-S.; Klingenhof, M.; Kroschel, M.; Paul, B.; Hübner, J.; Teschner, D.; Strasser, P. Catalyst−Support Surface Charge Effects on Structure and Activity of IrNi-Based Oxygen Evolution Reaction Catalysts Deposited on Tin-Oxide Supports. *Chem. Mater.* **2022**, *34* (21), 9350−9363.
(58) Smaali, K.; Guérin, D.; Passi, V.; Ordronneau, L.; Carella, A.; Mélin, T.; Dubois, E.; Vuillaume, D.; Simonato, J. P.; Lenfant, S. Physical Study by Surface Characterizations of Sarin Sensor on the Basis of Chemically Functionalized Silicon Nanoribbon Field Effect Transistor. *J. Phys. Chem. C* **2016**, *120* (20), 11180−11191.
(59) Uratani, H.; Yamashita, K. Charge carrier trapping at surface defects of perovskite solar cell absorbers: a first-principles study. *J. Phys. Chem. Lett.* **2017**, *8* (4), 742−746.
(60) Salatelli, E.; Marinelli, M.; Lanzi, M.; Zanelli, A.; Dell'Elce, S.; Liscio, A.; Gazzano, M.; Di Maria, F. Bulk Heterojunction Solar Cells: The Role of Alkyl Side Chain on Nanoscale Morphology of Sulfur Over-rich Regioregular Polythiophene/Fullerene Blends. *J. Phys. Chem. C* **2018**, *122* (8), 4156−4164.
(61) Di Maria, F.; Biasiucci, M.; Di Nicola, F. P.; Fabiano, E.; Zanelli, A.; Gazzano, M.; Salatelli, E.; Lanzi, M.; Della Sala, F.; Gigli, G.; et al. Nanoscale Characterization and Unexpected Photovoltaic Behavior of Low Band Gap Sulfur-Overrich-Thiophene/Benzothiadiazole Decamers and Polymers. *J. Phys. Chem. C* **2015**, *119* (49), 27200−27211.
(62) Ha, D.; Yoon, Y.; Park, I. J.; Cantu, L. T.; Martinez, A.; Zhitenev, N. Nanoscale Characterization of Photocurrent and Photovoltage in Polycrystalline Solar Cells. *J. Phys. Chem. C* **2023**, *127* (24), 11429−11437.
(63) Bai, X.; Wei, H.; Qiu, T.; Zhang, Z.; He, Y.; Wang, H. KPFM Study on the Charge Sign Reversal during Nanoscale Triboelectric Charging Induced by a Worn Tip and Sample Pretreatment. *J. Phys. Chem. C* **2021**, *125* (40), 22204−22213.
(64) Biere, N.; Koch, S.; Stohmann, P.; Walhorn, V.; Gölzhäuser, A.; Anselmetti, D. Resolving the 3D Orientation of Terphenylthiol Molecules on Noble Metals with Kelvin Probe Force Microscopy. *J. Phys. Chem. C* **2019**, *123* (32), 19659−19667.
(65) Grönbeck, H.; Barth, C. Revealing Carbon Phenomena at Palladium Nanoparticles by Analyzing the Work Function. *J. Phys. Chem. C* **2019**, *123* (7), 4360−4370.
(66) Nie, W.; Wang, X.; Wang, Z.; Gao, Y.; Chen, R.; Liu, Y.; Li, C.; Fan, F. Identifying the Role of the Local Charge Density on the Hydrogen Evolution Reaction of the Photoelectrode. *J. Phys. Chem. Lett.* **2021**, *12* (44), 10829−10836.
(67) Otoyama, M.; Yamaoka, T.; Ito, H.; Inagi, Y.; Sakuda, A.; Tatsumisago, M.; Hayashi, A. Visualizing Local Electrical Properties of Composite Electrodes in Sulfide All-Solid-State Batteries by Scanning Probe Microscopy. *J. Phys. Chem. C* **2021**, *125* (5), 2841−2849.
(68) Zhang, S.; Gao, L.; Song, A.; Zheng, X.; Yao, Q.; Ma, T.; Di, Z.; Feng, X.-Q.; Li, Q. Tuning local electrical conductivity via fine atomic scale structures of two-dimensional interfaces. *Nano Lett.* **2018**, *18* (9), 6030−6036.
(69) Zhang, L.; Roy, S. S.; Hamers, R. J.; Arnold, M. S.; Andrew, T. L. Molecular Orientation-Dependent Interfacial Energetics and Built-in Voltage Tuned by a Template Graphene Monolayer. *J. Phys. Chem. C* **2015**, *119* (1), 45−54.
(70) Yamamoto, S.; Taniguchi, D.; Okamoto, T.; Hirata, K.; Ozawa, T.; Fukuma, T. Nanoscale Corrosion Mechanism at Grain Boundaries of the Al−Zn−Mg Alloy Investigated by Open-Loop Electric Potential Microscopy. *J. Phys. Chem. C* **2023**, *127* (11), 5281−5288.

https://doi.org/10.1021/acs.jpcc.4c01461
J. Phys. Chem. C 2024, 128, 9813−9827